

## Electronic Supplementary Information

### Overcoming the Barrier of Conventional Electrochemical Deposition of Inorganic Composites

Ori Geuli and Daniel Mandler\*

Institute of Chemistry, the Hebrew University of Jerusalem, Jerusalem 9190401,  
Israel

#### Experimental Section

**HAp NPs synthesis:** 4.722 g of  $\text{Ca}(\text{NO}_3)_2$  (ACS EMSURE<sup>®</sup>, Merck) was dissolved in 18 mL of deionized water (18.3 M $\Omega$  cm, EasyPure UV, Barnstead) using a magnetic stirrer. The pH of the solution was adjusted to 12 by adding 0.6 mL ammonium hydroxide (25%, Baker Analyzed<sup>®</sup>, J.T Baker) and 17.4 mL of water. 1.584 g of  $(\text{NH}_4)_2\text{HPO}_4$  (BioUltra $\geq$ 99.0%, Sigma) was dissolved in 30 mL water while stirring. The pH of the solution was adjusted to 12 by adding 15 mL of concentrated ammonium hydroxide and another 19 mL of deionized water. The diammonium phosphate solution was slowly added dropwise using a separatory funnel to the calcium nitrate solution while vigorously stirring. The slow addition resulted in a turbid suspension. The latter was boiled for 1 h. Then, the suspension was cooled to room temperature and aged for 3 days. The precipitated NPs were washed with water and centrifuged at 10,000 rpm for 5 min. This was repeated three times. The HAp NPs precipitate was collected and freeze-dried. The HAp NPs were characterized by X-ray diffraction (XRD, Bruker, D9 Advance), X-ray photoelectron spectroscopy (XPS, Axis Ultra), high-resolution scanning electron microscopy (XHR-SEM, FEI Magellan<sup>™</sup> 400L), and high resolution transmission scanning electron microscopy (HR-TEM, Tecnai F20 G2). All XRD results were compared to the ICSD (Inorganic Crystal Structure Data) files.

**MoS<sub>2</sub> sheets synthesis:** 5 gr of  $\text{Na}_2\text{MoO}_4 \cdot 2\text{H}_2\text{O}$  (ACS reagent,  $\geq$ 99%) and 6 gr of thiourea (ACS reagent,  $\geq$ 99%) were dissolved in 60 mL of deionized water at room temperature for 30 min. After full dissolution of the precursors, the solution was transferred into 100 mL Teflon-lined vessel, which was placed inside stainless steel autoclave. The autoclave was placed inside preheated oven (at 200 °C) for 24 hours. The recovered black precipitates were washed in deionized water and centrifuged for

30 min at 10000 rpm. The washing process was repeated 3 times. The MoS<sub>2</sub> precipitates were collected and dried in an oven at 60 °C overnight in a vacuum oven. MoS<sub>2</sub> powder was obtained after manual milling of the dried clusters using mortar and pestle. The characterization of MoS<sub>2</sub> sheets was similar to that of HAp NPs.

**HAp NPs dispersion preparation:** HAp NPs dispersion was prepared by using polyethyleneimine (PEI, 50% in H<sub>2</sub>O, Sigma) as a stabilizing agent. Specifically, different amounts of HAp NPs (0.01, 0.05, 0.1, 0.2 and 0.4% wt) were added to 10 mM Zn(NO<sub>3</sub>)<sub>2</sub>·6H<sub>2</sub>O (ACS, Sigma-Aldrich) and PEI (0.05% wt) solution. 10 mM KNO<sub>3</sub> (EMSURE<sup>®</sup>, Merck) was added as supporting electrolyte. Stable HAp NPs dispersions were obtained after 30 min sonication using tip-sonicator (Sonics, Vibra Cell). The ζ-potential and the particles size distributions were determined as a function of pH using DLS (Zetasizer, Malvern ZS) by adding certain amounts of HCl (1M) or NaOH (1M).

**MoS<sub>2</sub> Sheets dispersion preparation:** HAp NPs dispersion was prepared by using polyethyleneimine (PEI, 50% in H<sub>2</sub>O, Sigma) as a stabilizing agent. Specifically, different amounts of MoS<sub>2</sub> sheets (0.1, 0.2 and 0.4% wt) were added to PEI (0.05% wt) solution. Stable HAp NPs dispersions were obtained after 60 min sonication using tip-sonicator (Sonics, Vibra Cell). After sonication certain volumes of Co(NO<sub>3</sub>)<sub>2</sub>·6H<sub>2</sub>O (ACS, Sigma-Aldrich) and KNO<sub>3</sub> (EMSURE<sup>®</sup>, Merck) aqueous solutions were added to obtain a concentration of 10 mM of each salt. The ζ-potential was determined as a function of pH using DLS (Zetasizer, Malvern ZS) by adding certain amounts of HCl (1M) or NaOH (1M).

**Titanium surface pretreatment:** Ti (Grade 4) plates were purchased from Bramil LTD. The surface area of the Ti plate was 1.08 cm<sup>2</sup>. The Ti plates were manually ground by grinding paper (grit 400, 600 and 1200, Microcut<sup>®</sup>, Buehler, USA) rinsed in acetone, ethanol and water in ultrasonic bath (Elmasonic P, Elma) for 10 min each, and etched in (30%)HF/(65%)HNO<sub>3</sub> (2 vol % and 20 vol %, respectively) for 1.5 min. After etching, the Ti plates were rinsed in copious amounts of water and dried under nitrogen flow. Commercial dental implants were kindly provided by SGS-Dental (Schaan, Liechtenstein).

**Ni foam activation:** Ni foam was activated by 10 min sonication in acetone and ethanol, each. After removing organic impurities, the Ni foam was sonicated in concentrated HCl solution for 5 min. It is important to mention that the temperature of sonication bath at this step was below 20 °C to avoid severe dissolution of Ni. After sonication in concentrated HCl, the Ni foam was washed and sonicated for additional 10 min in deionized water, followed by drying at 100 °C for 1 hr.

**Electrochemical deposition of HAp-ZnO composite:** ECD was carried out using a potentiostat (CHI 750B, CH Instruments) in a conventional three-electrode cell. Platinum wire (35 mm long) was used as a counter electrode, Ag/AgCl (sat.) as a reference electrode and pretreated Ti or commercial dental implant as a working electrode. For each experiment, a fresh 15 mL dispersion with different concentration of HAp NPs was used. The ECD was carried out at 70° C. A constant potential of -1.2 V was applied for 10 min. Then, the Ti surface was carefully withdrawn from the solution, dried at room temperature and gently washed with deionized water and dried again at room temperature. For pure ZnO coating, all the conditions were same, however, without adding HAp NPs and PEI. For pure HAp coating, the electrochemical deposition was carried out at 70 °C and the applied potential was -1.6 V for 10 min, where the HAp content was 0.4% wt and the aqueous solution contained 0.05% PEI and 20 mM KNO<sub>3</sub>. After deposition the Ti substrate was gently washed with deionized water and dried at room temperature.

**Coating characterization:** The coated substrates were analyzed by XRD ( $2\theta = 5-65^\circ$  at step size  $0.02^\circ \text{ s}^{-1}$  at). Quantitative phase content of the coatings was obtained by Rietveld analysis. High magnification images of the coated surface were taken by XHR-SEM. Cross-section images were obtained by SEM equipped with Focused ion beam (FIB). Element analysis was performed by XHR-SEM equipped with Energy-dispersive X-ray spectroscopy (EDS). Fourier transform infrared (FTIR) spectra were recorded with a Bruker Vertex 70v spectrometer in the reflection mode ( $80^\circ$ ) using a liquid-nitrogen-cooled mercury cadmium telluride (MCT) detector. The samples were scanned 1023 times with  $4 \text{ cm}^{-1}$  resolution. The spectra were recorded between 400 and  $4500 \text{ cm}^{-1}$ . MoS<sub>2</sub>-Co(OH)<sub>2</sub> different coatings were analyzed by X-ray photoelectron spectroscopy (XPS, Axis Ultra).

**Bioactivity test:** Simulated body fluid (SBF) was prepared according to a previous procedure<sup>1, 2</sup>. The coated implant was soaked in SBF solution at 37 °C for 4 weeks in a humidity chamber (Memmert, HCP 108). Every 5 days the SBF solution was replaced by a fresh one. The morphology of the implant was examined by XHR-SEM, XRD and EDS.

**Antibacterial activity:** *Escherichia Coli* (purchased from ATCC, USA) was used as a model bacteria for this study. A colony of E.coli was cultivated at 37 °C with shaking (120 rpm) in 15 mL of LB Broth (Lennox, Difco™, Fisher Scientific) overnight. The cell density of the bacterial suspension was adjusted to OD<sub>600</sub>= 0.3 by adding fresh LB Broth to the overnight cultivated suspension. A 10 µL aliquot of bacterial suspension was dropped on top of each coated Ti and allowed to incubate for 4 hrs in a 6 well plate under agitation (120 rpm). This was essential to ensure that all the bacteria settled on the coated substrate. After 4 hrs, the substrates were washed by adding 5 mL of LB Broth and the substrates were incubated with shaking (120 rpm) for additional 18 hrs. After incubation, 1.5 mL aliquot was analyzed spectrophotometrically (at 600 nm) in order to verify bacterial proliferation. The antibacterial tests were performed in triplicates and repeated at least two times.

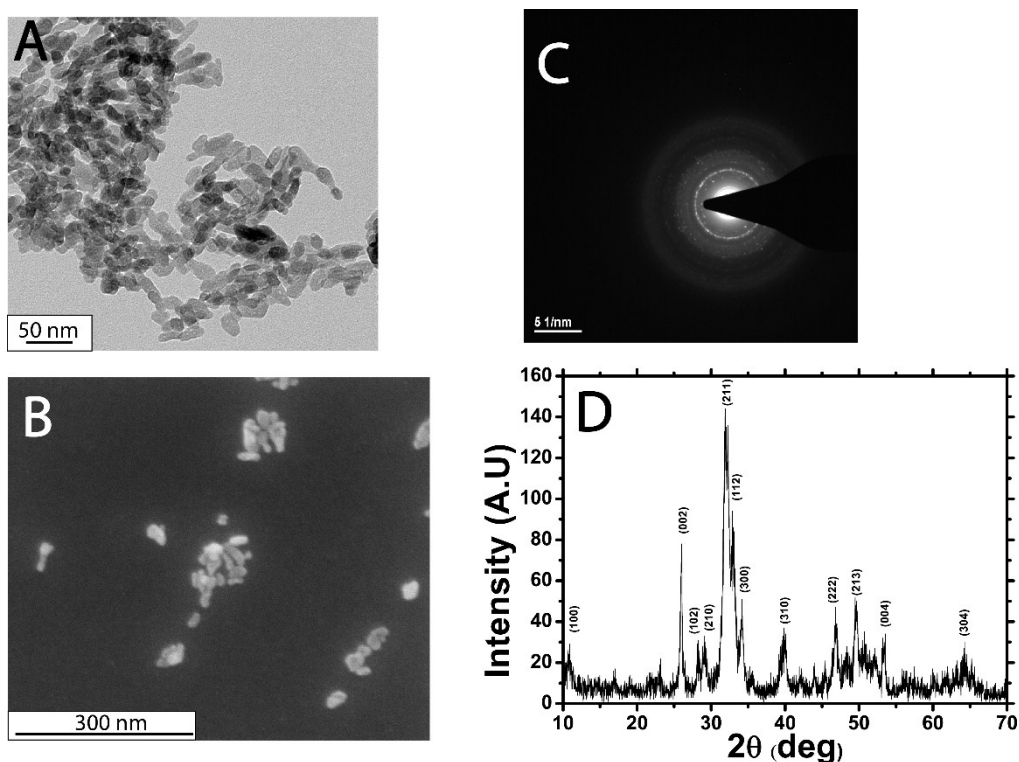
**Electrochemical deposition of MoS<sub>2</sub>-Co(OH)<sub>2</sub> composite:** ECD was conducted similarly to the HAp-ZnO apparatus with several adjustments. The working electrode was activated Ni foam, the applied potential was -1 V for 10 min and the ECD was carried out at room temperature. After deposition, the Ni foam was gently washed with deionized water and dried at ambient.

## Results

### HAp NPs characterization

HAp NPs were synthesized by a precipitation reaction between calcium and phosphate precursors. The molar ratio between Ca<sup>2+</sup> and PO<sub>4</sub><sup>3-</sup> was 1.67 in order to avoid phase impurities. SEM and TEM images (**Figure S1A, B**) show that HAp NPs have elongated shape, which is typical for HAp NPs synthesized by a wet chemical reaction.<sup>3-5</sup> The

average size based on TEM images was  $30\pm 8$  nm. Elemental analysis based on XPS (**Table S1**) showed that the NPs were composed of Ca, P, O and C. The high content of carbon is related to carbonaceous contaminations or carbonate substitution. The Ca/P ratio was 1.64, which is close to 1.67 of stoichiometric HAp. SAED-TEM pattern (**Figure S1C**) shows a typical diffraction of poly nanocrystalline HAp<sup>6</sup>. The XRD pattern (**Figure S1D**) shows the peaks of pure HAp (ICSD-PDF-01-084-1998) without any traces of other calcium phosphate phases. The calculated degree of crystallinity (based on XRD)



was 74%.<sup>7</sup>

**Fig. S1.** HAp NPs: A. TEM image; B. SEM image; C. SAED-TEM diffraction pattern and D. XRD pattern.

**Table S1.** XPS element analysis of HAp NPs.

Element	At %
Ca	$16.8\pm 0.8$
P	$9.6\pm 0.1$
O	$58.0\pm 0.9$

C	15.4±1.0
---	----------

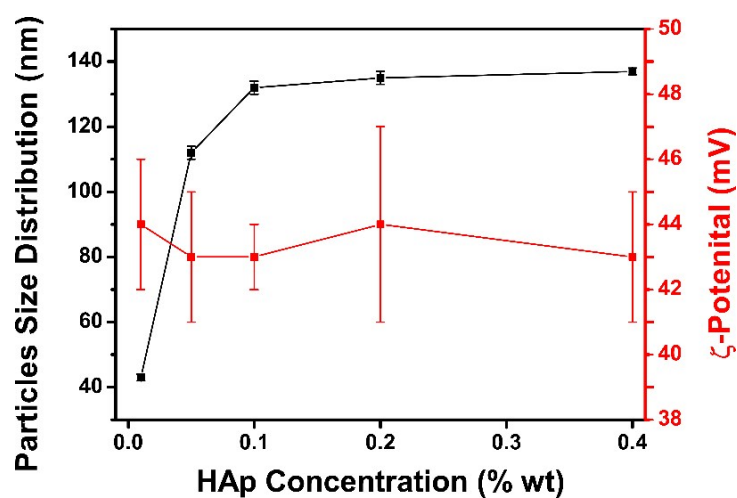
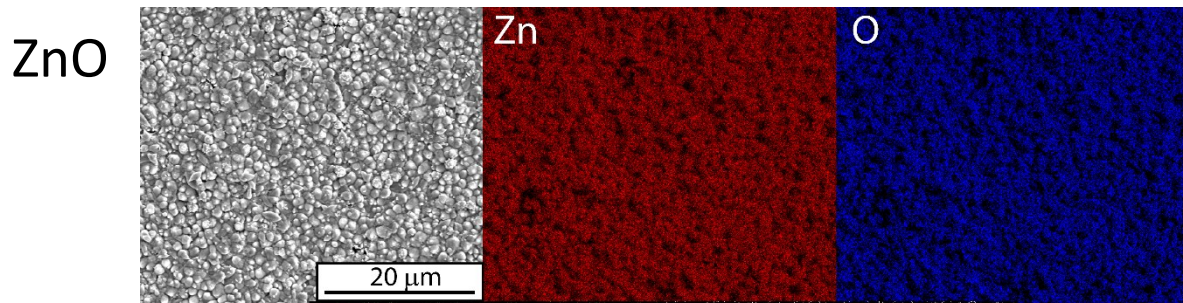
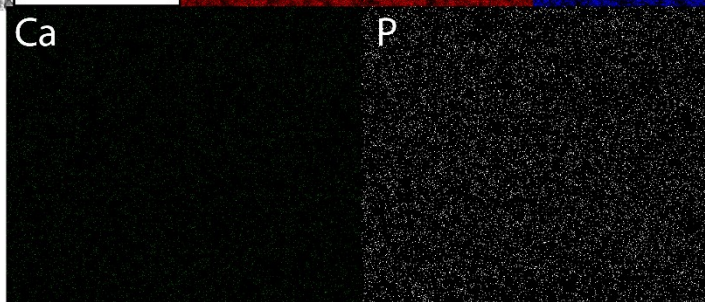


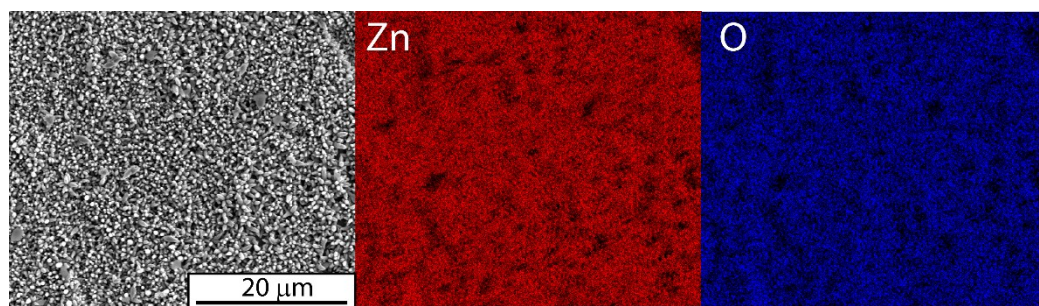
**Fig. S2.** Particles size distribution and  $\zeta$ -potential measurements of different concentrations of HAp NPs dispersed by PEI in  $\text{Zn}(\text{NO}_3)_2$  (10 mM) and  $\text{KNO}_3$  (10 mM) aqueous solution.



Element	% At
Zn	47.2±0.9
O	52.0±0.7
Cl	0.7±0.21



0.01% HAp



Element	% At
Zn	39.3±2.2
O	50.0±0.5
Ti	8.8±1.6
Ca	1.08±0.03
P	0.8±0.04

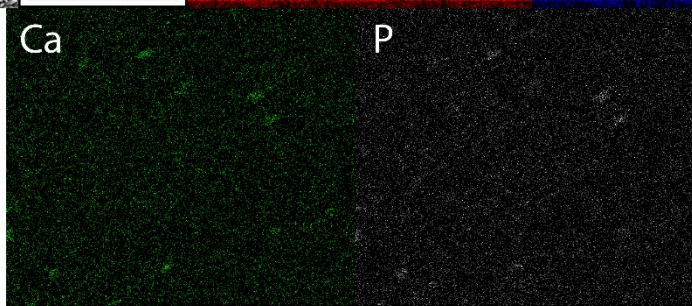
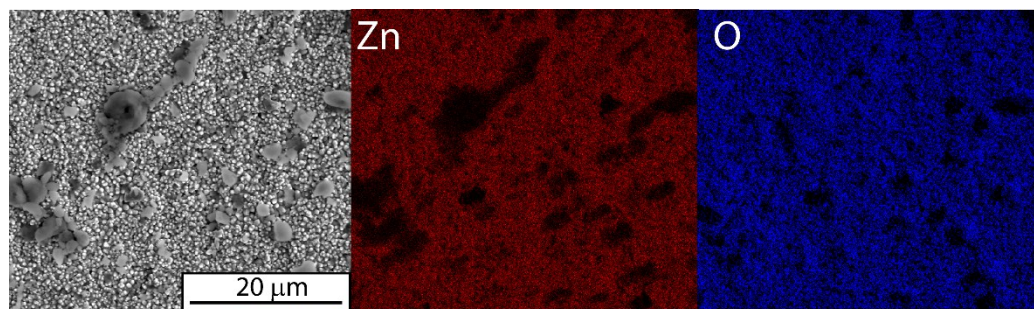
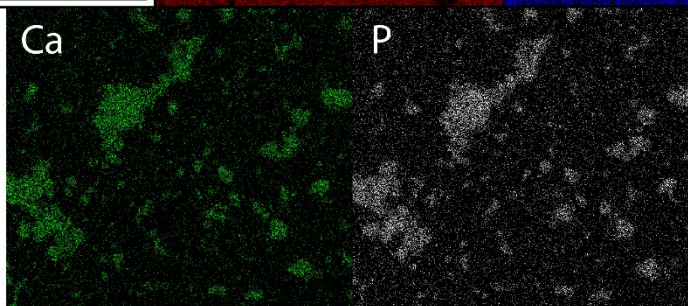


**Fig. S3.** A. EDS element analysis and elemental mapping of ZnO, ZnO-HAp and HAp co-ECD composite coatings with different concentrations of HAp NPs.

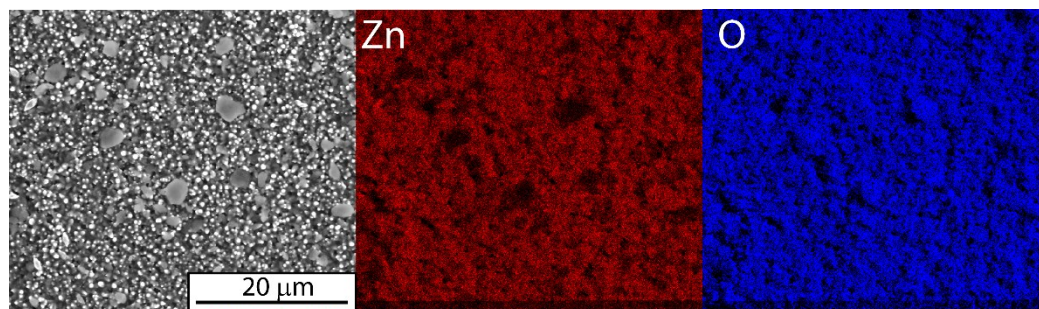
0.05% HAp



Element	% At
Zn	38.2±2.0
O	51.5±1.7
Ti	5.6±3.0
Ca	2.0±0.5
P	1.8±0.5
C	4.9±0.4



0.1% HAp



Element	% At
Zn	28.8±0.4
O	51.9±0.8
Ti	4.2±2.5
Ca	5.7±1.0
P	4.4±0.7
C	5.5±0.5

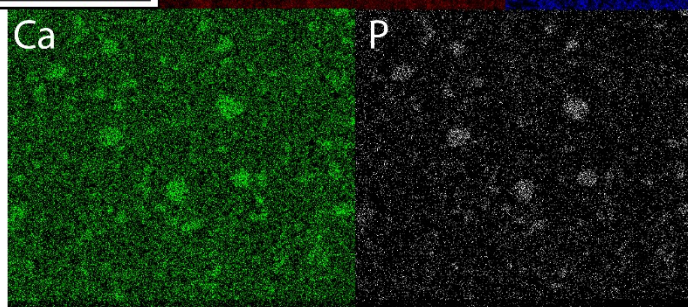
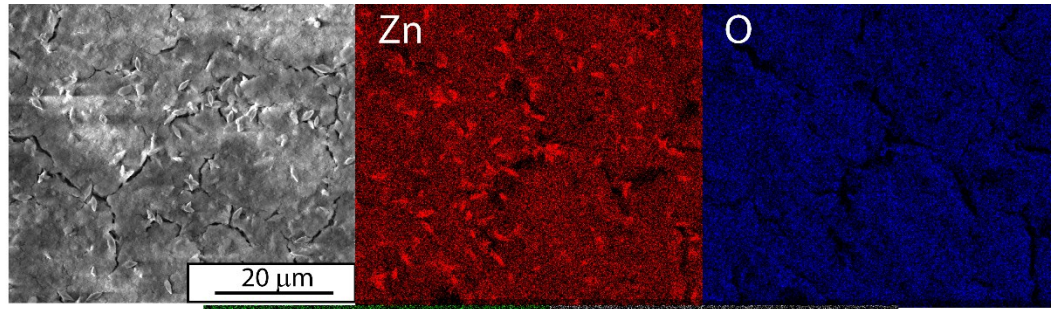
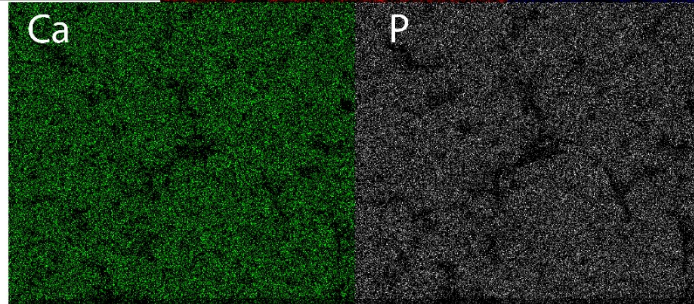


Fig. S3. A. Continued from previous page.

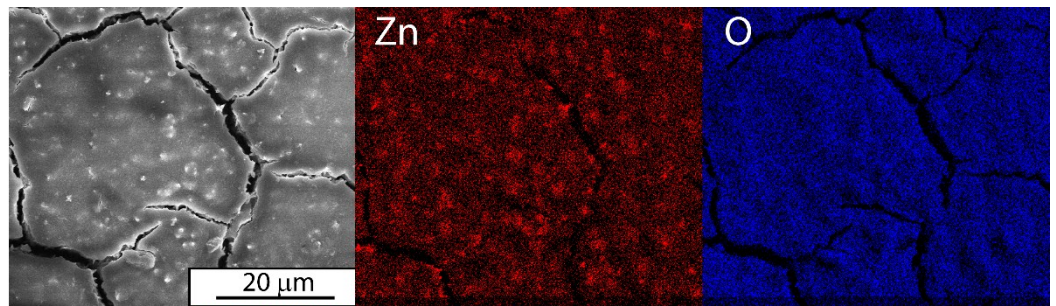
0.2% HAp



Element	% At
Zn	13.5±0.2
O	59.3±0.1
Ti	1.1±0.2
Ca	11.5±0.4
P	9.0±0.3
C	4.4±0.1



0.4% HAp



Element	% At
Zn	6.5±1.4
O	59.6±1.4
Ti	0.7±0.1
Ca	15.1±0.4
P	11.3±0.4
C	7.1±0.5

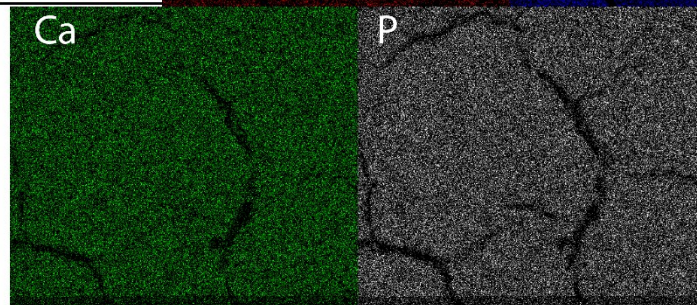


Fig. S3. A. Continued from previous page.

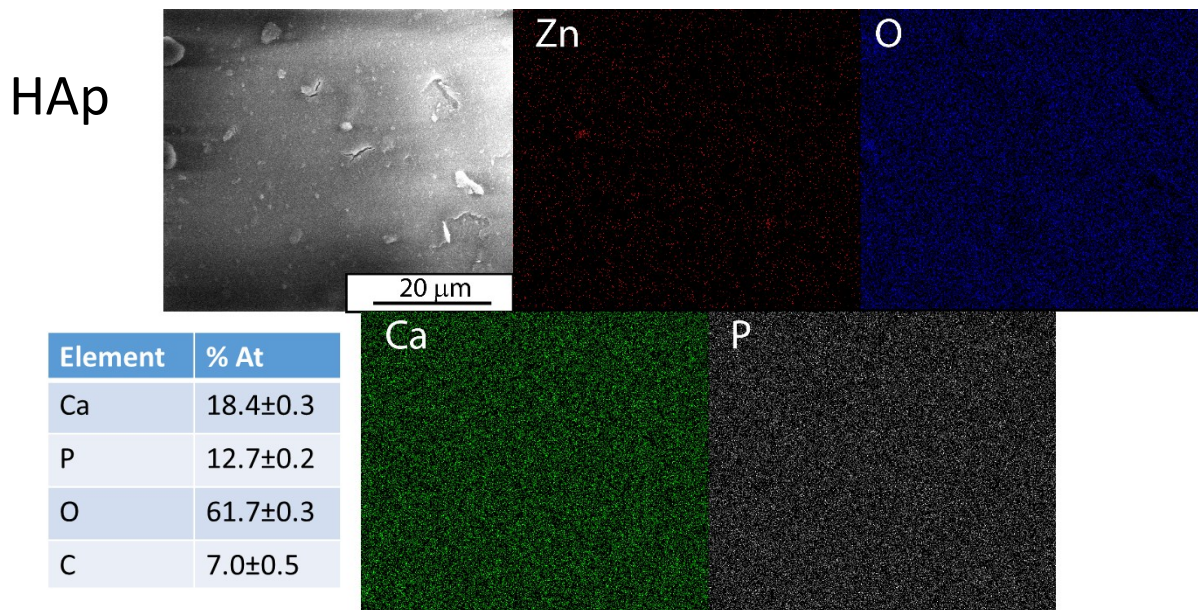


Fig. S3. A. Continued from previous page.

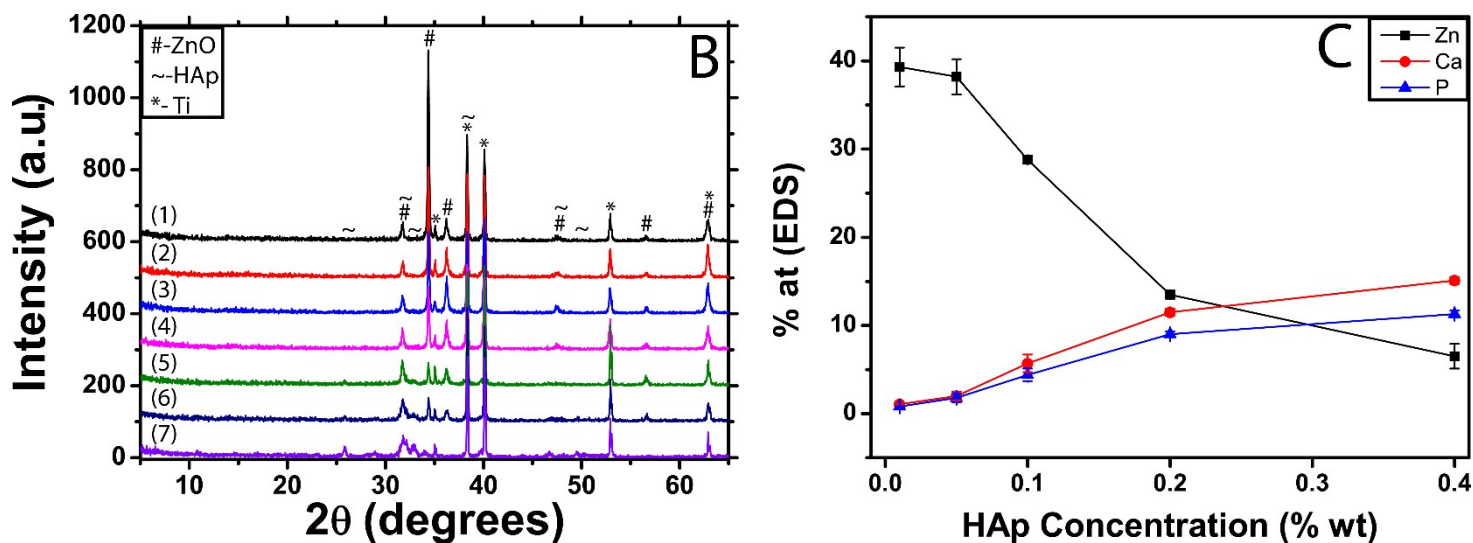


Fig. S3. B. XRD of: (1) pure ZnO, (2-6) ZnO-HAp coatings with different HAp content (0.01, 0.05, 0.1, 0.2 and 0.4% wt.) and (7) of pure HAp NPs, respectively. C. %at. (measured by EDS) of Zn, Ca and P as a function of HAp concentration (% wt.) in the ZnO-HAp deposits. Potential and time of deposition were  $-1.2$  V and 10 min, respectively except for the pure HAp where the potential was  $-1.6$  V.

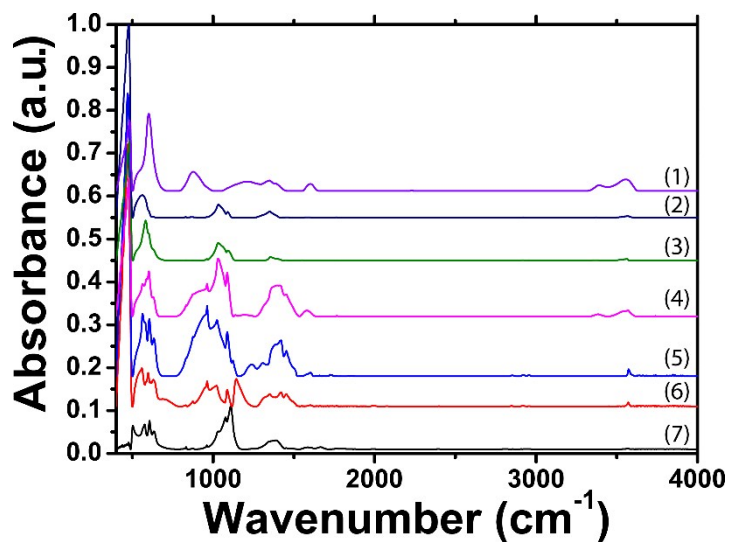
The XRD pattern (Fig. 2B) of the different coatings verifies that only well-crystallized ZnO with a hexagonal Wurtzite structure (ICSD-PDF-01-089-7102) were deposited without any traces of impurities, suggesting a good electrochemical compatibility with HAp. Fig. 2C shows the %at. (by EDS) of Zn, Ca and P, which indicates that the ratio between ZnO and HAp can be precisely tailored. These results demonstrate the novelty of our process, where in addition to the ability to electrochemically co-deposit two substances, their ratio can be conveniently adjusted. One of the advantages of this approach lies in the ability to pre-synthesize the NPs in different shapes, which are maintained in the deposit.

Dispersion	Phase Content (%wt)- XRD	
	ZnO	HAp
0% wt HAp	100	0
0.01% wt HAp	100	BDL
0.05% wt HAp	100	BDL
0.1% wt HAp	66	34
0.2% wt HAp	33	67
0.4% wt HAp	19	81

**Table S2.** Phase composition based on XRD Rietveld analysis of different ZnO-HAp composites (\*BDL=below detection level).

Fig. S4 shows the FTIR spectra of ZnO-HAp coatings. The characteristic peaks of ZnO are shown at 480, 600 and 3550  $\text{cm}^{-1}$ . The two intense peaks between 400 and 600  $\text{cm}^{-1}$  are belong to metal-oxide [M-O] stretching vibration <sup>8-10</sup>. The peak at 3550  $\text{cm}^{-1}$  belongs to OH group <sup>11</sup>. The peaks at 881 and 1385  $\text{cm}^{-1}$  may be related to nitrate adsorption <sup>11, 12</sup>. The peaks at 1607 and 3380  $\text{cm}^{-1}$  attributed to water adsorption of atmospheric moisture <sup>12</sup>. The typical peaks of HAp are shown at 472, 501, 571, 605, 961, 1031, 1078 and 1109  $\text{cm}^{-1}$ , which are attributed to  $\text{PO}_4^{3-}$  vibrations <sup>13, 14</sup>. The peaks at 631 and 3570  $\text{cm}^{-1}$  are attributed to OH group <sup>15</sup>. The peaks at 874 and 1387  $\text{cm}^{-1}$  are related to carbonate impurities <sup>13</sup>. The peaks at 1457 and 1583  $\text{cm}^{-1}$  belongs N-H bending vibrations <sup>16, 17</sup> and the peak at 1308  $\text{cm}^{-1}$  is assigned to C-N vibrations of PEI. The two small peaks between 2800 and 3000  $\text{cm}^{-1}$  are associated with -CH

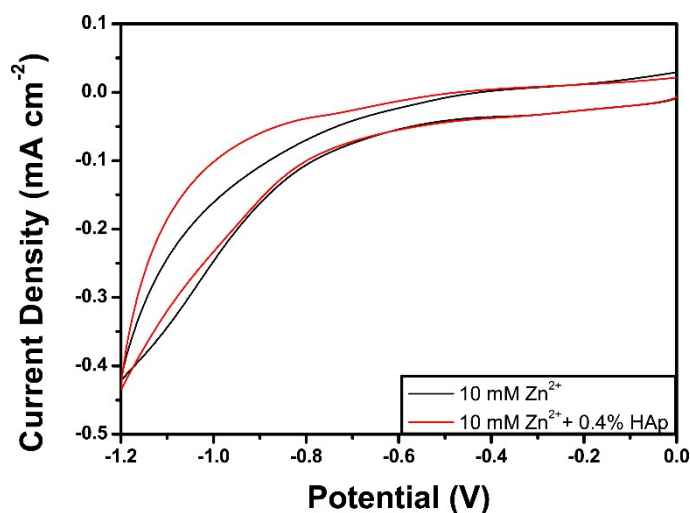
stretching vibrations <sup>18, 19</sup>. It can be seen that the characteristic peaks of HAp are intensified when greater amount of HAp NPs was deposited. As evidence, the FTIR spectra of ZnO-HAp (0.1-0.4%) clearly shows the typical peaks of PO<sub>4</sub><sup>3-</sup> vibrations. On the other hand, the intense peak of M-O vibrations at 470 cm<sup>-1</sup> is clearly shown in all



ZnO-HAp coatings regardless to HAp content. This phenomenon is associated with the absorption band, which is dependent on the morphology, crystallinity and the size of ZnO <sup>8, 20, 21</sup>.

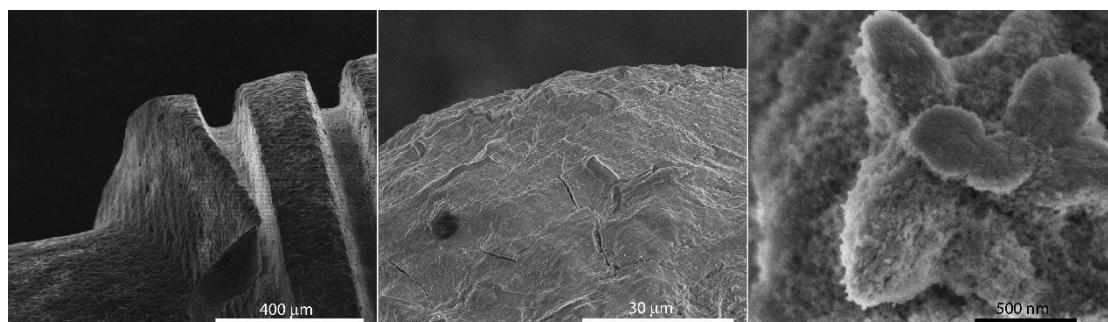
**Fig. S4.** FTIR spectra of: (1) pure ZnO, (7) HAp, and (2-6) ZnO-HAp coatings with different HAp concentrations (0.01, 0.05, 0.1, 0.2 and 0.4% wt), respectively.

Fig. S5 shows the cyclic voltammetry curves of  $Zn^{2+}$  solution with and without HAp. It can be seen that the addition of HAp has no effect on the deposition of ZnO as the CV with and without HAp are similar. Hence, we can propose that the deposition of HAp by destabilization of the positively charged polymeric shell and the reaction between the dissolved Zn ions with the generated hydroxyl ions at the electrode surface to form insoluble compound, display good electrochemical compatibility.



**Fig. S5.** Cyclic voltammetry of 10 mM  $Zn(NO_3)_2$  with and without HAp.  $KNO_3$  (10 mM) was added as supporting electrolyte to both systems.

**Fig. S6.** SEM images at different magnifications of a dental implant electrochemically coated from 0.4% wt. HAp NPs dispersion and 10 mM  $Zn(NO_3)_2$ . Potential and time of deposition are as in Fig. 2.



## Bioactivity Test

Preliminary assessment of the bioactive nature of ZnO-HAp composite coating was carried out *in-vitro* using SBF solution. The guiding principal behind the SBF study is to evaluate the ability of coatings to enhance the precipitation of inorganic species, such as Ca, P, Mg, Na and Cl from the aqueous media, which resembles the biomineralization process of the coated implant *in-vivo*<sup>1, 2</sup>. HAp as the main inorganic component of human bone has been intensively applied as a bioactive agent of biomedical implants to induce implant-bone interactions. Fig. S7A-D shows SEM images of ZnO-HAp (0.4% wt), HAp and ZnO coatings and bare Ti after 4 weeks immersion in SBF solution at 37±1 °C. A different morphology was obtained when pure-HAp was immersed in SBF, where nano-needles were formed. This morphology is typical for HAp layers after continuous exposure to SBF<sup>1, 2, 22</sup>. Interestingly, pellet-like clusters were formed on top of the ZnO-HAp (0.4% wt) and ZnO coatings, suggesting that a Zn-substituted bone-like apatite layer was formed. These results indicate that both the crystallinity and the morphology of the precipitate is highly dependent on several parameters, such as: pH, temperature, ionic strength and composition<sup>22, 23</sup>. Zn has been reported as inhibitor for HAp crystallization by boundary grains segregation, which explains the different structure of precipitated HAp in the presence of ZnO. Lin Du *et al* explained this phenomenon by Zn ions adsorption on the nucleation sites of HAp, which results in lower nucleation rate and increased agglomeration on active growth sites<sup>24</sup>. Similar morphologies of HAp agglomeration from SBF solution in the presence of Zn were also reported in other systems<sup>25, 26</sup>. Precipitation of inorganic film did not occur on top of bare Ti, indicating the poor bioactivity of Ti. EDS element analysis of ZnO-HAp (0.4% wt), ZnO, HAp and bare Ti is provided in Fig. S7A-D. The incorporation of inorganic ions, such as Mg<sup>2+</sup>, Na<sup>+</sup> and Cl<sup>-</sup>, resembles the biomineralization of the coating *in-vivo*. It can be seen that the biomineralization process occurred at all the coated Ti. Obviously, no significant inorganic content, besides traces of carbonaceous impurities, was detected on bare Ti. Considerable amounts of Ca and P that were detected in the ZnO coating, show the interesting ability of ZnO to nucleate calcium-phosphate precipitation. Mg<sup>2+</sup> and Cl<sup>-</sup> were detected in both HAp and ZnO-HAp coatings. Further inspection was carried out

by XRD analysis (Fig. S7A-D). The XRD of ZnO shows only the typical pattern of crystalline ZnO without any indication of other materials. This result may be related to the insufficient amounts of precipitate that can be detected by XRD. The XRD pattern of pure HAp shows intensification of the diffraction peaks at (002), (211), (112), (300), (310), (222) and (213) planes. This indicates on the nucleation and crystallization of HAp on top of the electrochemically deposited layer. The XRD of ZnO-HAp shows mainly the peaks of HAp, where the peaks of ZnO are hardly detected. In addition, the XRD pattern implies that the ZnO-HAp layer became more amorphous as compared with the HAp coating. This can be explained by the generation of  $Zn^{2+}$  ions as a result of ZnO dissolution, which ultimately led to inferior HAp crystallization. Fig. S7E shows a cross-section image of ZnO-HAp (0.4% wt) after 4 weeks immersion in SBF at  $37 \pm 1$  °C. It can be seen, that the precipitation of bone minerals occurred in a cluster-like formation, which was non-homogenously scattered across the coated substrate. Elemental mapping shows that both the coating and the SBF precipitated clusters are composed mainly of the same elements, where the presence of Pt is associated with the sputtering of a protection layer during the FIB cutting.

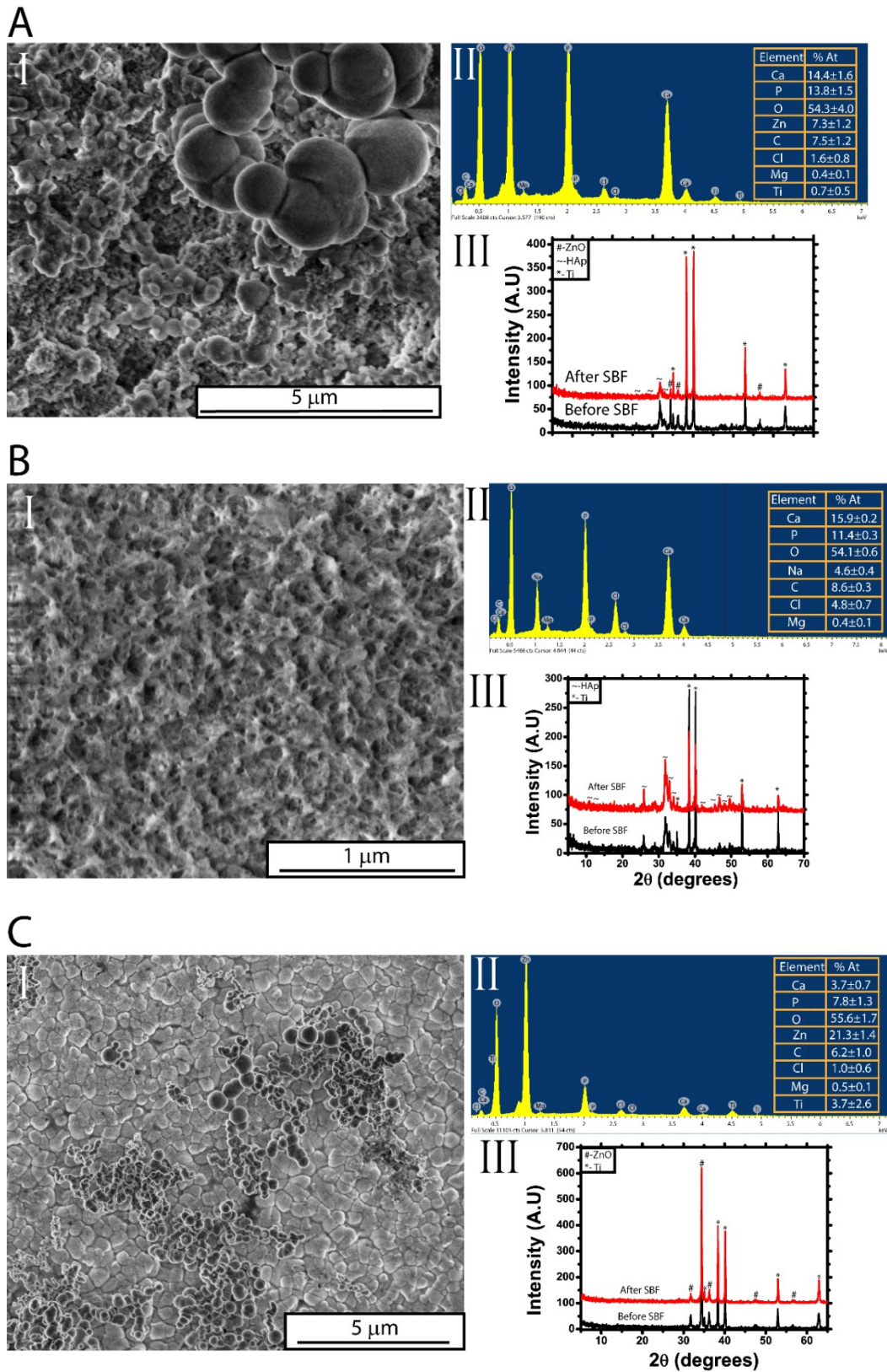
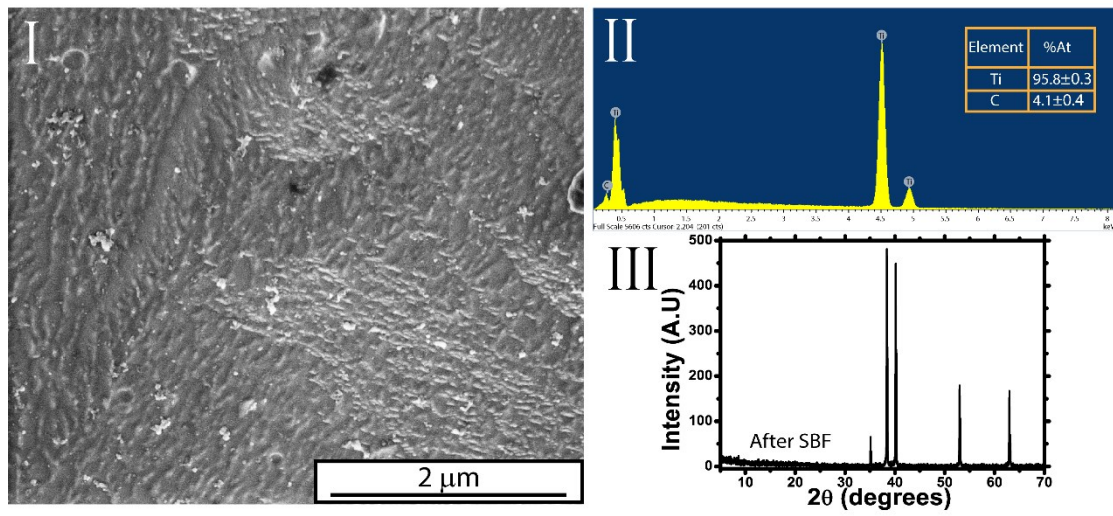


**Fig. S7.** SEM (I), EDS spectrum, element analysis (II) and XRD pattern (III) of ZnO-HAp (0.4%) (A), HAp (B), ZnO (C) and bare Ti (D) after 4 weeks of immersion at 37 °C in SBF. Cross-section SEM image and the corresponding EDS mapping of ZnO-HAp (0.4%) (E) after the SBF immersion experiment.

D



E

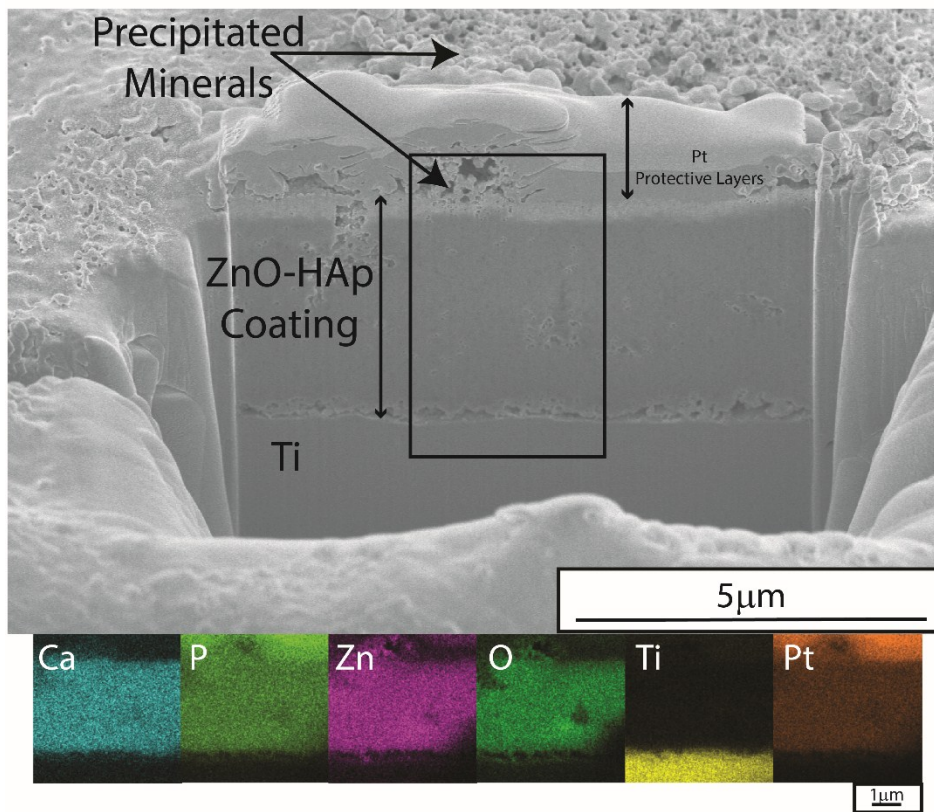
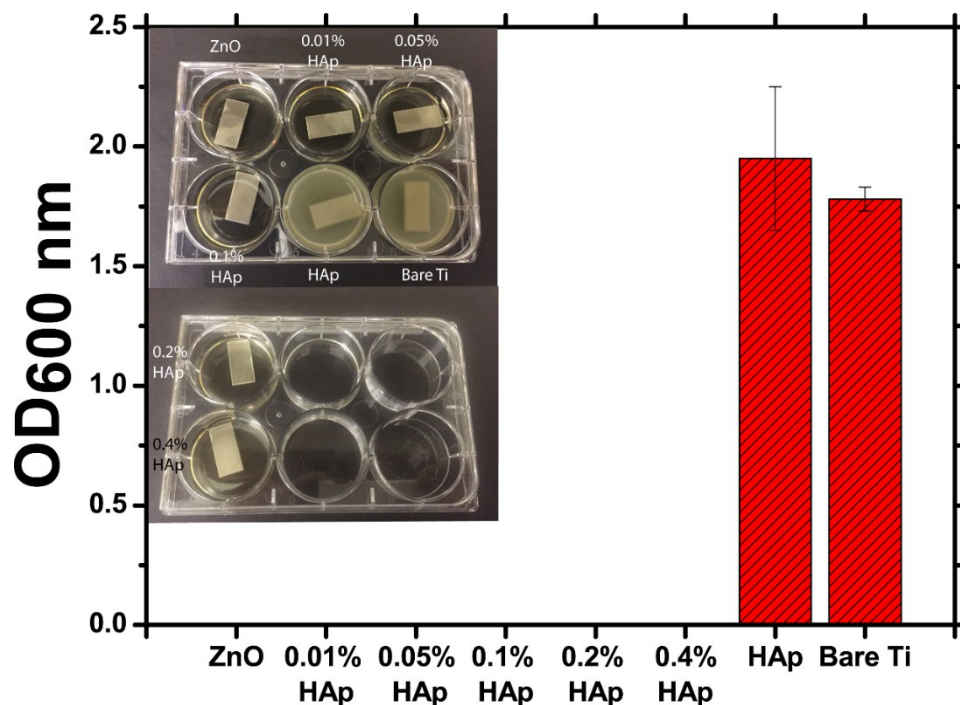


Fig. S7. Continued from previous page.

## Antibacterial Study

Fig. S8 shows the antibacterial activity of ZnO-HAp coatings, which was evaluated against *E.coli* bacteria. ZnO is a well-known bactericidal agent, which has a "contact killing" effect upon bacteria attachment<sup>27</sup>. We carried out this experiment for 18 hours in order to reach the stationary phase of the bacteria after the exponential growth. We used ZnO-HAp coatings with different concentration of HAp. Pure ZnO, HAp and bare Ti were used as control experiments. In all ZnO-HAp coatings no bacterial proliferation was observed in the growth medium, indicating the eradication of the bacteria. As evidence, the solution remained clear and the OD<sub>600</sub> was 0.00 compared to sterilized growth medium. For HAp coatings and bare Ti, after 18 hrs incubation, the growth mediums were very opaque, which clearly indicated on bacterial growth. Although, HAp was electrochemically deposited with PEI, which is considered as an antibacterial agent, its minute amount could not evoke any bactericidal activity. This result indicates that ECD of HAp NPs is only accompanied with traces of PEI. These remarkable results show that even at low concentration of



ZnO, less than 20% wt, efficient antibacterial activity was observed.

**Fig. S8.** Absorbance measurement (at 600 nm) of bacterial growth medium after 4 hrs contact of bacterial culture with different coatings, followed by 18 hrs incubation in growth medium at 37° C.

### **MoS<sub>2</sub> hydrothermal synthesis:**

MoS<sub>2</sub> sheets were synthesized by reacting sodium molybdate with thiourea as a sulfur donor. Under hydrothermal conditions, i.e. high temperature and pressure, thiourea is decomposed, while releasing H<sub>2</sub>S and NH<sub>3</sub> that react with the dissolved MoO<sub>4</sub><sup>2-</sup> to form MoS<sub>2</sub><sup>28</sup>. Fig. S9A shows a SEM image of the synthesized MoS<sub>2</sub> sheets. It can be seen that the sheets are aggregated into a 3D flower-like structure, which is in agreements with previous reports<sup>29-31</sup>. The XRD pattern (Fig. S9B) shows a typical pattern of MoS<sub>2</sub> with diffraction peaks at 33°, 44°, and 59°, assigned to the (101), (103), and (110) planes of hexagonal phase MoS<sub>2</sub> (ICSD-PDF-89-5112), respectively. However, the diffraction peak corresponding to (002) plane at 14° is split into two diffraction peaks at 9.2° and 17.8° (label as (002)\* and (004)\*, respectively). This finding indicates on an increased interlayer spacing<sup>32</sup>. This spacing of standard MoS<sub>2</sub> is 0.615 nm, where the calculated interlayer spacing using the Scherrer equation of the synthesized MoS<sub>2</sub> is 0.914 nm, which is notably bigger corresponding to an expansion in the interlayer spacing of 0.299 nm. This phenomenon is ascribed to the intercalation of small size ions, such as Na<sup>+</sup> or NH<sub>4</sub><sup>+</sup>, which originate from the precursors<sup>32-34</sup>. The phase identification was further studied by XPS (Fig. S9C, D). The Mo 3d spectrum shows the typical peaks of semiconducting MoS<sub>2</sub> that is composed of two peaks located at 229.4 and 232.5 eV, and are assigned to the 3d<sub>5/2</sub> and 3d<sub>3/2</sub>, of Mo<sup>4+</sup>, respectively<sup>35</sup>. The XPS spectrum of S reveals two main peaks at 162.3 and 163.5 eV, which correspond to 2p<sub>3/2</sub> and 2p<sub>1/2</sub> of S<sup>2-</sup>, respectively. The two small peaks at 169.8 and 171.0 eV are attributed to SO<sub>2</sub> impurities as a possible byproduct of thiourea decomposition or oxidation of S by atmospheric oxygen. The Mo/S ratio based on EDS element analysis is 0.48, which is relatively close to the theoretical value (0.5).

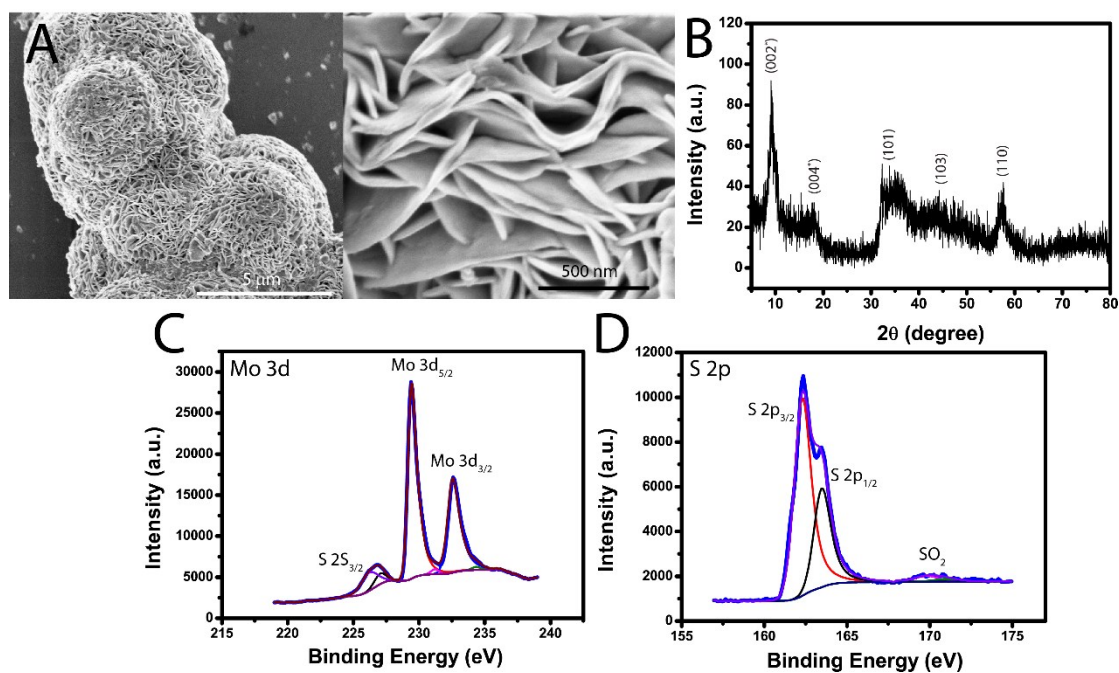


**Fig. S9.** A SEM images in different magnifications and B. XRD pattern of hydrothermally synthesized MoS<sub>2</sub> sheets. C and D. XPS spectra of Mo 3d and S 2p, respectively.

Sample	ζ-Potential (mV)
MoS <sub>2</sub> in water	-40±5
MoS <sub>2</sub> + PEI in water	51±3

**Table S3.** ζ-potential measurements of pristine MoS<sub>2</sub> with and without the addition of PEI in water.

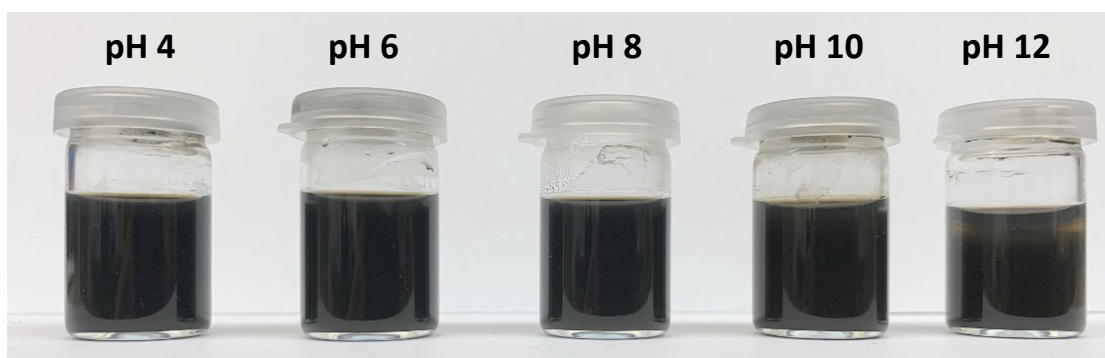
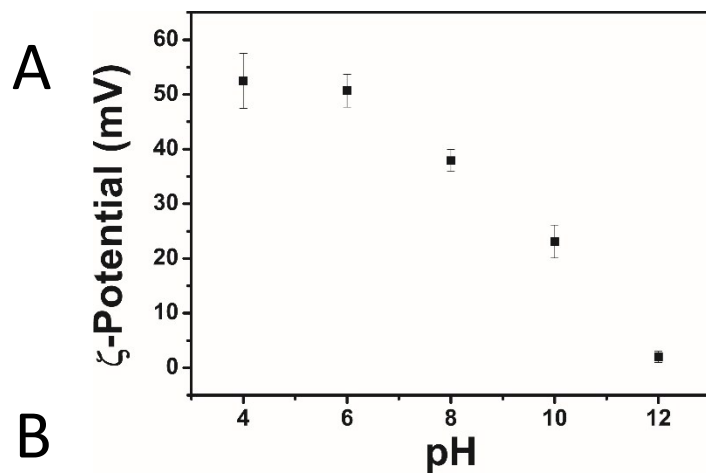


**Fig. S10.** A.  $\zeta$ -Potential measurements of MoS<sub>2</sub> sheets dispersed by PEI in 10 mM KNO<sub>3</sub> solution. B. Image of a series PEI-stabilized MoS<sub>2</sub> sheets dispersions at different pH.

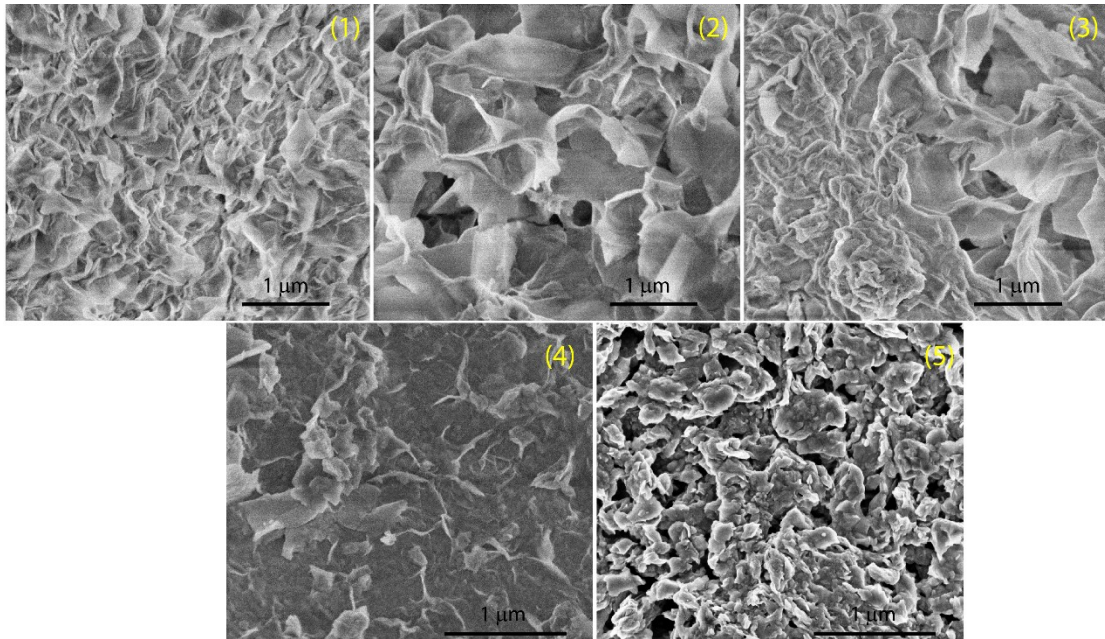


**Fig. S11.** SEM images of: (1) pure  $\text{Co(OH)}_2$ , (2-4)  $\text{MoS}_2\text{-Co(OH)}_2$  coatings with different  $\text{MoS}_2$  content (0, 1, 0.2 and 0.4% wt.) and (5) of pure  $\text{MoS}_2$ , respectively.

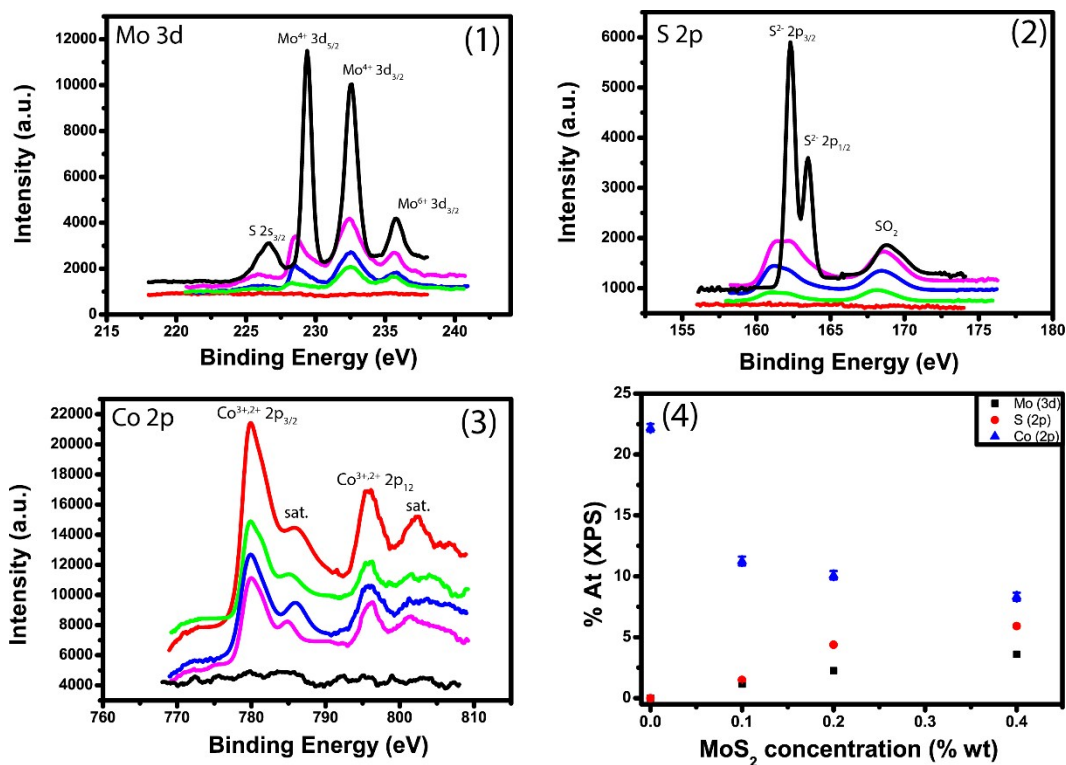


**Fig. S12.** XPS spectra of Mo 3d (1), S 2p (2) and Co 2p (3) of  $\text{Co(OH)}_2$  (red),  $\text{MoS}_2$  (black) and  $\text{MoS}_2\text{-Co(OH)}_2$  coatings (green, blue and pink) assigned with 0.1, 0.2, 0.4% wt, respectively, of  $\text{MoS}_2$  dispersed in 10 mM  $\text{Co(NO}_3)_2$  aqueous solution.

Fig. S13 shows the CV curves of 10 mM  $\text{Co}^{2+}$  solution with and without different concentrations of dispersed  $\text{MoS}_2$  sheets. Generally, it can be seen that the addition of  $\text{MoS}_2$  has no effect on the reduction of water that occurs at potentials greater than  $-0.6$  V. Hence, we can assume that there is no competition between the two processes, namely deprotonation of the amine shell of the PEI-stabilized  $\text{MoS}_2$  and the concurrent deposition of  $\text{Co}(\text{OH})_2$ . It seems that during the scan back towards the positive direction, namely between  $-0.4$ - $0$  V, there is increase in the current. This incline in the current might be attributed to pseudocapacitance of  $\text{MoS}_2$ <sup>36, 37</sup>, which associated with fast intercalation of  $\text{K}^+$  ions as described in the following reaction<sup>38</sup>:

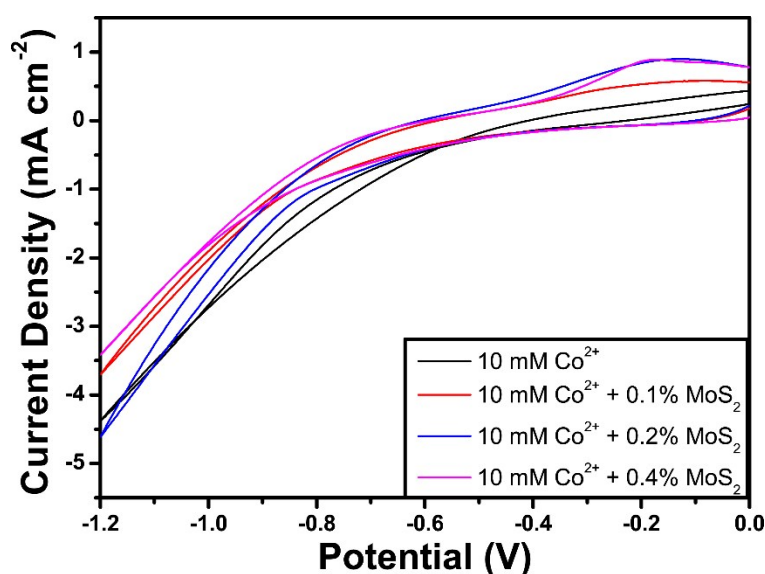


**Fig. S13.** Cyclic voltammetry curves of 10 mM  $\text{Co}(\text{NO}_3)_2$  with different concentrations of  $\text{MoS}_2$ .  $\text{KNO}_3$  (10 mM) was added as supporting electrolyte for both system.

#### References:

1. P. N. Chavan, M. M. Bahir, R. U. Mene, M. P. Mahabole and R. S. Khairnar, *Materials Science and Engineering B-Advanced Functional Solid-State Materials*, 2010, **168**, 224-230.
2. T. Kokubo and H. Takadama, *Biomaterials*, 2006, **27**, 2907-2915.
3. M. Wei, A. Ruys, B. Milthorpe and C. Sorrell, *Journal of Materials Science: Materials in Medicine*, 2005, **16**, 319-324.
4. M. Wei, A. Ruys, B. Milthorpe, C. Sorrell and J. Evans, *Journal of Sol-Gel Science and Technology*, 2001, **21**, 39-48.

5. M. Wei, A. J. Ruys, B. K. Milthorpe and C. C. Sorrell, *Journal of Materials Science-Materials in Medicine*, 2005, **16**, 319-324.
6. E. Suvorova and P. Buffat, *Journal of microscopy*, 1999, **196**, 46-58.
7. E. Landi, A. Tampieri, G. Celotti and S. Sprio, *Journal of the European Ceramic Society*, 2000, **20**, 2377-2387.
8. A. Anžlovar, Z. C. Orel, K. Kogej and M. Žigon, *Journal of Nanomaterials*, 2012, **2012**, 31.
9. N. Senthilkumar, E. Nandhakumar, P. Priya, D. Soni, M. Vimalan and I. V. Potheher, *New Journal of Chemistry*, 2017, **41**, 10347-10356.
10. H. Kumar and R. Rani, *International Letters of Chemistry, Physics and Astronomy*, 2013, **14**, 26--36.
11. D. Gopi, N. Murugan, S. Ramya and L. Kavitha, *Journal of Materials Chemistry B*, 2014, **2**, 5531-5540.
12. K. Singh, A. A. Ibrahim, A. Umar, A. Kumar, G. Chaudhary, S. Singh and S. Mehta, *Sensors and Actuators B: Chemical*, 2014, **202**, 1044-1050.
13. L. Berzina-Cimdina and N. Borodajenko, *Research of calcium phosphates using Fourier transform infrared spectroscopy*, INTECH Open Access Publisher, 2012.
14. M. Corno, C. Busco, B. Civalleri and P. Ugliengo, *Physical Chemistry Chemical Physics*, 2006, **8**, 2464-2472.
15. H. Zeng and W. R. Lacefield, *Biomaterials*, 2000, **21**, 23-30.
16. F. Wang, P. Liu, T. Nie, H. Wei and Z. Cui, *International journal of molecular sciences*, 2012, **14**, 17-29.
17. S. Tan, M. Erol, A. Attygalle, H. Du and S. Sukhishvili, *Langmuir*, 2007, **23**, 9836-9843.
18. H. Shi, L. Xue, A. Gao, Y. Fu, Q. Zhou and L. Zhu, *Journal of Membrane Science*, 2016, **498**, 39-47.
19. A. Ortega, S. Farah, P. Tranque, A. V. Ocaña, S. H. Nam-Cha, N. Beyth, C. Gómez-Roldán, R. Pérez-Tanoira, A. J. Domb and F. C. Pérez-Martínez, *IET nanobiotechnology*, 2015, **9**, 342-348.
20. L. Wu, Y. Wu, X. Pan and F. Kong, *Optical Materials*, 2006, **28**, 418-422.
21. Z. Yang, X. Zong, Z. Ye, B. Zhao, Q. Wang and P. Wang, *Biomaterials*, 2010, **31**, 7534-7541.
22. T. Kobayashi, S. Ono, S. Hirakura, Y. Oaki and H. Imai, *CrystEngComm*, 2012, **14**, 1143-1149.
23. N. Spanos, D. Misirlis, D. Kanellopoulou and P. Koutsoukos, *Journal of materials science*, 2006, **41**, 1805-1812.
24. R. L. Du, J. Chang, S. Y. Ni, W. Y. Zhai and J. Y. Wang, *Journal of biomaterials applications*, 2006, **20**, 341-360.
25. N. Iqbal, M. R. A. Kadir, N. H. Mahmood, N. Salim, G. R. Froemming, H. Balaji and T. Kamarul, *Ceramics International*, 2014, **40**, 4507-4513.
26. S. Miao, W. Weng, K. Cheng, P. Du, G. Shen, G. Han and S. Zhang, *Surface and Coatings Technology*, 2005, **198**, 223-226.
27. J. Pasquet, Y. Chevalier, J. Pelletier, E. Couval, D. Bouvier and M.-A. Bolzinger, *Colloids and Surfaces A: Physicochemical and Engineering Aspects*, 2014, **457**, 263-274.
28. X.-L. Li and Y.-D. Li, *The Journal of Physical Chemistry B*, 2004, **108**, 13893-13900.
29. X. Leng, Y. Wang and F. Wang, *Advanced Materials Interfaces*, 2019, 1900010.
30. H. Li, K. Yu, H. Fu, B. Guo, X. Lei and Z. Zhu, *The Journal of Physical Chemistry C*, 2015, **119**, 7959-7968.
31. Y. Yuan, H. Lv, Q. Xu, H. Liu and Y. Wang, *Nanoscale*, 2019, **11**, 4318-4327.
32. D. Wang, Y. Xiao, X. Luo, Z. Wu, Y.-J. Wang and B. Fang, *ACS Sustainable Chemistry & Engineering*, 2017, **5**, 2509-2515.

33. N. Feng, R. Meng, L. Zu, Y. Feng, C. Peng, J. Huang, G. Liu, B. Chen and J. Yang, *Nature communications*, 2019, **10**, 1372.
34. K. D. Rasamani, F. Alimohammadi and Y. Sun, *Materials Today*, 2017, **20**, 83-91.
35. Y. Jiao, A. M. Hafez, D. Cao, A. Mukhopadhyay, Y. Ma and H. Zhu, *Small*, 2018, **14**, 1800640.
36. M. Acerce, D. Voiry and M. Chhowalla, *Nature nanotechnology*, 2015, **10**, 313.
37. W. Choi, N. Choudhary, G. H. Han, J. Park, D. Akinwande and Y. H. Lee, *Materials Today*, 2017, **20**, 116-130.
38. R. Wang, S. Wang, X. Peng, Y. Zhang, D. Jin, P. K. Chu and L. Zhang, *ACS applied materials & interfaces*, 2017, **9**, 32745-32755.